

11121  
113995

**NASA TECHNICAL MEMORANDUM 107620**

P.34

**ENVIRONMENTAL FATIGUE OF AN Al-Li-Cu  
ALLOY: PART II - MICROSCOPIC HYDROGEN  
CRACKING PROCESSES**

**Robert S. Piascik and Richard P. Gangloff**

**MAY 1992**



**National Aeronautics and  
Space Administration**

**Langley Research Center  
Hampton, Virginia 23665**

(NASA-TM-107620) ENVIRONMENTAL  
FATIGUE OF AN Al-Li-Cu ALLOY. PART  
2: MICROSCOPIC HYDROGEN CRACKING  
PROCESSES (NASA) 34 p

N92-31214

Unclass

G3/39 0113995



# ENVIRONMENTAL FATIGUE OF AN Al-Li-Cu ALLOY: PART II - MICROSCOPIC HYDROGEN CRACKING PROCESSES

Robert S. Piascik and Richard P. Gangloff<sup>1</sup>

## ABSTRACT

*Based on a fractographic analysis of fatigue crack propagation (FCP) in Al-Li-Cu alloy 2090 stressed in a variety of inert and embrittling environments, microscopic crack paths are identified and correlated with intrinsic  $da/dN$ - $\Delta K$  kinetics. FCP rates in 2090 are accelerated by hydrogen producing environments (pure water vapor, moist air and aqueous NaCl), as defined in Part I. For these cases, subgrain boundary fatigue cracking (SGC) dominates for  $\Delta K$  values where the crack tip process zone, a significant fraction of the cyclic plastic zone, is sufficiently large to envelop  $5 \mu\text{m}$  subgrains in the unrecrystallized microstructure. SGC may be due to strong hydrogen trapping at  $T_1$  precipitates concentrated at subboundaries. At low  $\Delta K$ , the plastic zone diameter is smaller than the subgrain size and FCP progresses along  $\{100\}$  planes due to either local lattice decohesion or aluminum-lithium hydride cracking. For inert environments (vacuum, helium and oxygen), or at high  $\Delta K$  where the hydrogen effect on  $da/dN$  is small, FCP is along  $\{111\}$  slip planes; this mode does not transition with increasing  $\Delta K$  and plastic zone size. The SGC and  $\{100\}$  crystallographic cracking modes, and the governing influence of the crack tip process zone volume ( $\Delta K$ ), support hydrogen embrittlement rather than a surface film rupture and anodic dissolution mechanism for environmental FCP. Multi-sloped  $\log da/dN$ - $\log \Delta K$  behavior is produced by changes in process zone hydrogen-microstructure interactions, and not by purely micromechanical-microstructure interactions, in contradiction to microstructural distance-based fatigue models.*

---

<sup>1</sup>Robert S. Piascik, formerly a graduate student in the Department of Materials Science at the University of Virginia, is a Scientist in the Mechanics of Materials Branch at the NASA-Langley Research Center, Hampton, VA, 23665. Richard P. Gangloff is Professor of Materials Science and Engineering at the University of Virginia, Charlottesville, VA, 22903.

## I. INTRODUCTION

The development of advanced Al-Li-X alloys for damage tolerant applications requires kinetics data and mechanism-based predictive models for environmentally assisted fatigue crack propagation (FCP). Research reported in Part I<sup>(1)</sup> characterized FCP in precipitation strengthened Al-Li-Cu alloy 2090 in controlled inert (vacuum and helium), gaseous oxygen, and hydrogenous (pure water vapor, moist air and aqueous NaCl with varying polarization) environments. These experiments established intrinsic crack growth rate ( $da/dN$ ) versus stress intensity range ( $\Delta K = K_{max} - K_{min}$  at a stress ratio,  $R = K_{min}/K_{max}$ ) data that are independent of crack closure and nonsteady-state chemical effects. On this basis, the environmental cracking resistance of 2090 is substantial and similar to the behavior of commercial 2000 series alloys. Gaseous and aqueous environments none-the-less enhance FCP in alloy 2090, as qualitatively explained by hydrogen environment embrittlement<sup>(1,2)</sup>.

Determinations of microscopic fatigue fracture modes or paths are necessary to refute or further establish the hydrogen mechanism for crack tip process zone damage, and ultimately to develop a predictive model of  $da/dN$ - $\Delta K$  laws. The objective of the work reported in Part II is to physically define the microscopic processes for environmental fatigue crack tip damage in Al-Li-Cu alloys. The approach is to correlate the crack growth rate response for alloy 2090 in various inert and aggressive environments (Part I<sup>(1)</sup>) with fractographic observations of crack path and the underlying microstructure. The results of this analysis are employed in Part III to develop a crack tip hydrogen damage model of  $da/dN$ - $\Delta K$ <sup>(3)</sup>.

### A. Background

For aluminum alloys in inert gaseous environments, or at high  $\Delta K$  and rapid  $da/dN$  where environmental effects are minimal, fatigue crack surface morphologies include mechanical striation, precipitate free zone shear, planar slip band separation and ductile rupture<sup>(4-13)</sup>. Only limited fractographic studies have been conducted on fatigue crack surfaces in aluminum alloys stressed in truly inert environments. Results for fatigue in laboratory air reflect the influence of hydrogen.

Unique crack surface morphologies are associated with hydrogen environment enhanced fatigue crack propagation (FCP) in precipitation hardened aluminum alloys; including intergranular separation, crystallographic "cleavage", "brittle striations" and slip band cracking<sup>(1,9,10,14-22)</sup>. Early studies of Paris-regime FCP identified brittle striated crack growth in an Al-Zn-Mg alloy

cycled in sea water<sup>(10,12,13,17)</sup>. In contrast to blunting-buckling-based mechanical striations<sup>(6)</sup>, each repeating brittle striation involves crack growth on or near {100} or {110} planes and is characterized as "cleavage fracture". For lower  $\Delta K$ , FCP produces large crystallographic facets for a variety of environments, including moist air<sup>(1,9,14,16,20)</sup>. Facets were identified as hydrogen promoted "cleavage" parallel to {100}<sup>(4)</sup> and as slip band cracking, presumably along {111} planes<sup>(9,12)</sup>. Both high angle and subgrain boundaries are possible paths for environment enhanced FCP<sup>(10,14,21,22)</sup>. Fractographic support has not been presented to establish dissolution dominated corrosion fatigue in water vapor or electrolytes<sup>(23,24)</sup>.

While under-to peak-aged aluminum alloys can exhibit both planar and homogeneous deformation, fatigue damage in commonly studied Al-Li-X alloy-moist air systems is generally believed to be controlled by mechanisms related to heterogeneously localized planar slip<sup>(6,25,26)</sup>. Slip is concentrated because mobile dislocations readily shear Al-Li based precipitates, including ordered  $\delta'$  ( $\text{Al}_3\text{Li}$ ) and perhaps  $T_1$  ( $\text{Al}_2\text{CuLi}$ ) when present with  $\delta'$ , and accentuated by strong crystallographic texture<sup>(25,27)</sup>. FCP proceeds along these highly strained regions, parallel to {111} slip planes, and causes a planar "twist" morphology that is the source of pronounced crack closure<sup>(25,26,28-30)</sup>.

While localized planar slip is undoubtedly important, little is known about environmental effects on microscopic fatigue crack paths and causal damage mechanisms in Al-Li alloys. Kinetics data are limited for FCP in inert environments with insignificant water vapor and oxygen contamination, and fatigue crack paths are not typically characterized in detail as a function of intrinsic  $\Delta K$ , independent of crack closure effects<sup>(31-35)</sup>. Al-Li-Cu alloys exhibit tortuously transgranular slip band cracking (SBC) for FCP in moderate vacuum and moist air, at least for intermediate to high  $\Delta K$ <sup>(25,26,28-31,35)</sup>. Yoder et al. confirmed {111} slip plane cracking for highly textured alloy 2090 in moist air and qualitatively described the transgranular fracture morphology produced in aqueous chloride as being less tortuous<sup>(28,30,31)</sup>. Although unlikely, this result is attributed to anodic dissolution of the large fracture surface asperities produced by slip plane cracking. Chen and Duquette demonstrated that hydrogen enhances {111} slip plane cracking in a binary Al-Li alloy which exhibits atypically strong slip localization<sup>(36)</sup>. Ohrloff et al. reported {111} slip plane cracking for FCP in alloy 2091 stressed in either vacuum or aqueous NaCl, with multiple slip plane facets and faster growth rates created by dislocation transport of hydrogen from the chloride source to within the crack tip process zone<sup>(34)</sup>. The sigmoidal shape of the  $da/dN$ - $\Delta K$  relationship for the 2091/moist air

system was qualitatively related to a change in the microscopic fracture mode with increasing  $\Delta K$ <sup>(34)</sup>. The role of unrecrystallized subgrain and high angle grain boundaries, with  $T_1$  and  $T_2$  ( $Al_6CuLi_3$ ) precipitates, in hydrogen environment FCP damage mechanisms is unclear. The occurrence of transgranular {001} crystallographic cracking and the effect of stress intensity range on the dominant crack path have not been systematically determined for Al-Li alloys.

## II. EXPERIMENTAL PROCEDURE

Alloy 2090 plate (38 mm thick) was studied in the solution treated, stretched (6%) and peak aged (4 hours at 190°C) condition.<sup>2</sup> Only longitudinal-transverse (L-T) oriented fatigue cracks are considered here. Since the Part I experiments were conducted at constant  $\Delta K$  and  $R$ , well defined intervals of fatigue crack extension were available for microscopic analysis<sup>(1)</sup>. Crack surfaces were characterized using a JEOL-35 scanning electron microscope (SEM) operated in the secondary electron mode. Initial SEM examinations were performed without chemical cleaning or gold sputtering of the fracture surfaces. When surface charging affected resolution at high magnification, oxide and corrosion debris were removed by a two minute ultrasonic cleaning in acetone, by sputter deposition of gold, or by both methods.

A microetch-pitting technique was used to identify the crystallographic orientation of fatigue fracture surface facets<sup>(4,5)</sup>. The fracture surface was etched at 25°C for 3 seconds in a solution composed of 50 ml  $H_2O$ , 50 ml  $HNO_3$ , 32 ml  $HCl$  and 2 ml  $HF$ . After etching, the fracture surface was immediately flushed with distilled water and dried by clean compressed air. Pit geometry is related to etch revealed and intersecting crystallographic planes<sup>(5)</sup>. This technique reveals cracking along {111} slip planes as equilateral triangular pits, along {100} planes as square pits, and along {110} planes as rectangular pits.

## III. RESULTS

### A. *Material Characterization*

The mechanical properties and chemistry of peak aged alloy 2090 were previously reported<sup>(37)</sup>. Optical microscopy indicates that the 2090 plate is unrecrystallized. Average high angle grain sizes are 10 mm, 3.3 mm and 110  $\mu m$  in the longitudinal, transverse and thickness

---

<sup>2</sup>To enhance boundary precipitation of  $T_1$  and  $T_2$ , aging is performed at 190°C; this temperature is higher than typical peak aging practice which involves 140°C to 165°C for times on the order of 10 to 30 hours.

directions, respectively.

X-ray texture analysis of the 38 mm thick 2090 plate at the T/4 and T/2 thickness positions confirms the lack of recrystallization.  $\{111\}$  pole figures are shown in Figure 1. These results indicate two components of the fcc "brass" deformation texture,  $\{110\} \langle 112 \rangle$ , at the T/2 location.<sup>3</sup> A cube texture,  $\{100\} \langle 001 \rangle$ , typical of recrystallization is not evident at the T/2 location, consistent with optical and electron microscopy. At the T/4 location, the deformation texture is present, but is less well defined and some recrystallization cube texture may be present. Interpretation of the texture in Figure 1 is complicated by the presence of the  $\{112\} \langle 111 \rangle$  and  $\{123\} \langle 412 \rangle$  components, particularly at the T/4 location. These results are consistent with the alloy 2090 texture reported by Yoder et al.<sup>(28,30)</sup>. Single edge crack fatigue specimens were machined about the T/3 location<sup>(3)</sup>.

Transmission electron microscopy (TEM) of stretched and peak aged alloy 2090 confirmed that the plate microstructure is unrecrystallized and identified three matrix precipitates;  $\delta'$  ( $\text{Al}_3\text{Li}$ ),  $T_1$  ( $\text{Al}_2\text{CuLi}$ ) and  $\Theta'$  ( $\text{Al}_2\text{Cu}$ ); and  $T_1$  on subgrain boundaries. The micrograph of the TS plane in Figure 2a illustrates the unrecrystallized subgrain microstructure. Average subgrain sizes are 12  $\mu\text{m}$  (longitudinal), 5  $\mu\text{m}$  (transverse) and 3  $\mu\text{m}$  (thickness). Subgrain sizes in the important transverse direction ranged from 1 to 10  $\mu\text{m}$ . Figure 2b is a bright field micrograph showing the uniform distribution of  $T_1$  and  $\delta'$  within a subgrain, and the nonuniform distribution of  $T_1$  at a subgrain boundary (arrows). The dark field micrograph in Figure 2c shows (arrows)  $T_1$  along the subgrain boundary in the area of Figure 2b. In Figure 2d a decrease in  $\delta'$  is observed at the subgrain boundary from Figure 2b, suggesting that subgrain boundary  $T_1$  precipitation results in a small  $\delta'$  depleted zone<sup>(38)</sup>. Large  $T_2$  ( $\text{Al}_6\text{CuLi}_3$ ) precipitates and  $\delta'$  precipitate free zones (PFZ) were noted along high angle grain boundaries. The  $\delta'$ -PFZ contained a uniform distribution of  $T_1$  and  $\Theta'$ .

The aqueous chloride corrosion behavior of alloy 2090 is reported elsewhere<sup>(37,39)</sup>. The free corrosion and breakaway potentials are equal ( $-700 \text{ mV}^4$ ) for aerated 1% (neutral) NaCl, and are  $-1000 \text{ mV}$  and  $-700 \text{ mV}$ , respectively, for 2090 in helium deaerated solution. Constituent particles ( $\text{Al}_7\text{Cu}_2\text{Fe}$ ) and subgrain boundary  $T_1$  are sites of localized pitting that was

---

<sup>3</sup>This notation denotes that a  $\{110\}$ -type plane is parallel to the rolling surface and a  $\langle 112 \rangle$ -type direction in this plane is parallel to the rolling or longitudinal direction.

<sup>4</sup>All electrode potentials are referenced to the saturated calomel electrode (SCE).

observed at potentials 100 mV anodic to the deaerated open circuit potential, but well cathodic of the pitting breakaway potential, similar to recent results<sup>(40,41)</sup>. Localized attack of  $T_1$  at subgrain boundaries is illustrated by the SEM images of the LT plane in Figure 3. The etched but unexposed surface (Figure 3a) reveals the subgrain structure. Comparison with an unetched surface (Figure 3b), exposed to 0.1% NaCl for 84 hours at -1000 mV, demonstrates localized attack at sites along low angle grain boundaries. Examination at higher magnification shows attack at discrete regions aligned along subgrain boundaries. Since only  $T_1$  precipitates on subgrain boundaries, this phase is a likely site for localized corrosion.  $T_1$  is active in NaCl and dissolves preferentially in the cathodic aluminum matrix<sup>(41,42)</sup>.

### ***B. Crack Paths for FCP in Vacuum, Helium and Oxygen Environments***

The fatigue fracture surfaces for alloy 2090 in purified inert (vacuum and helium) and oxygen environments are similar. Fatigue cracks propagate along  $\{111\}$  slip planes, forming a crack path that is tortuous and dominated by "twist" deflections<sup>(43)</sup>. Slip band cracking (SBC) is observed at all levels of  $\Delta K$  without evidence of striations. This result is consistent with the facts that macroscopic FCP rates are equivalent and slow for 2090 in these environments, and that the  $da/dN-\Delta K$  relationship is a single power law to relatively low growth rates<sup>(1)</sup>.

**1. Vacuum and Helium:** The tortuous fatigue crack surface produced in helium is shown by the SEM fractograph in Figure 4a. The crack grew from the notch at the bottom to the top of the figure as indicated by the arrow. The numbers on the right indicate regions of constant  $\Delta K$  (10.6 MPa $\sqrt{m}$ , 16.2 MPa $\sqrt{m}$  and 2.4 MPa $\sqrt{m}$  from 1 to 3, respectively), as identified by electrical potential measurements of crack length<sup>(1)</sup>. The fracture surface morphology does not vary with  $\Delta K$ . Figure 4a shows that FCP at each level of  $\Delta K$  proceeds along a tortuous path, exhibiting severe planar deflections that form deep troughs parallel to the crack growth direction ("twist" morphology). Figure 4b is a transverse section (metallographically polished and Keller's etched) along line A-A in Figure 4a, revealing the faceted fatigue surface for the helium environment. Intersections of planar facets are characterized by included angles ranging from 55° to 65°. Yoder and coworkers concluded that, based on the texture of alloy 2090, these facets are produced by  $\{111\}$  slip band cracking<sup>(28,30)</sup>. Etch pit analysis of the facet surfaces revealed triangular pits, as demonstrated in Figure 5 for the 2090-vacuum case, confirming that fatigue crack propagation in inert environments is along  $\{111\}$  slip planes.

While the fatigue cracks in Figure 4b are parallel to  $\{111\}$  planes, the crystallographic details of FCP are unclear. Potential high angle grain boundaries are marked by arrows in

Figure 4b. The fact that the slip band crack crosses darkly etched boundaries, with little change in direction, indicates that these adjacent "grains" are similarly oriented and of the same texture component. It is unclear why similarly oriented (presumably low angle) boundaries are prominently etched and sized on the order of high angle grains (110  $\mu\text{m}$ ). The original work by Yoder and coworkers did not consider the various deformation textures and the likelihood that slip preferentially occurs on high Schmid factor planes in 2090. It is possible that the apex angle of the facet is explained based on cracking parallel to either intersecting texture components, hence at a high angle grain boundary, or intersecting  $\{111\}$  planes of similar Schmid factor in a single texture component, hence at a low angle grain boundary.

The regions outlined in Figure 4a include areas of subgrain boundary failure. The subgranular regions exhibit evidence of tearing, similar to that observed for tensile overload fracture (Figure 8b). Presumably, small ligaments of material remain between the fatigue slip plane cracks. These regions are not favorably oriented for SBC and fail along subgrain boundaries due to locally high tensile stress. Additionally, localized mechanical subgrain cracking may be due to a heterogeneous distribution of boundary  $T_1$ . Presumably, this phase governs intersubgranular microvoid fracture.

**2. Oxygen:** The fatigue surfaces produced in oxygen at two constant  $\Delta K$  levels (10.6  $\text{MPa}\sqrt{\text{m}}$  and 16.2  $\text{MPa}\sqrt{\text{m}}$ ) exhibit a tortuous "twist" morphology similar to that observed for alloy 2090 in vacuum and helium, Figure 6. Etch pit analysis identified the planar asperity surfaces as parallel to  $\{111\}$  planes.

At high magnification, a difference in the slip band crack surface appearance is observed for oxygen compared to vacuum. The vacuum fracture surface exhibits a metallic and smooth crystallographic appearance, while the oxygen surface exhibits a roughened texture and a dark grey-black color. Auger microprobe analysis verified that an oxide film forms on the alloy 2090 crack surface during fatigue cracking in pure oxygen, but not in vacuum or helium<sup>(37)</sup>. In spite of the presence of the crack surface oxide, equal rates of FCP and predominantly  $\{111\}$  cracking for the oxygen and vacuum environments establish that  $\text{O}_2$  has no effect on crack tip fatigue damage.

### **C. Crack Paths for FCP in Hydrogen Producing Environments**

In contrast to the behavior in vacuum, helium and oxygen, environmentally enhanced FCP in the hydrogen producing environments (water vapor, moist air and aqueous NaCl) is substantial and proceeds along either subgrain boundaries or  $\{100\}$  planes, depending on  $\Delta K$

and environment activity. Crystallographic {100} "cleavage" cracking is dominant at low  $\Delta K$ , while intersubgranular cracking (SGC), with small regions of {111} slip plane cracking, is observed at higher  $\Delta K$ . For NaCl, subgrain boundary cracking persists to lower  $\Delta K$  levels compared to moist air or pure water vapor. Transitions in fracture mode correlate with the complex shape of  $da/dN$ - $\Delta K$  relationships observed for the hydrogen environments<sup>(1)</sup>.

**1. Water Vapor:** FCP in saturation exposure water vapor<sup>(1)</sup> produces a flat crack surface, Figure 7, that exhibits different microscopic modes compared to tortuous SBC observed for the vacuum, helium and oxygen environments (Figures 4 and 6). At high  $\Delta K$  (16 MPa $\sqrt{m}$  and area A in Figure 7), the fatigue surface consists primarily of subgrain boundary cracking, Figure 8a. The features in this fractograph are similar in size to the subgrains observed by TEM, Figure 2a.

Intersubgranular fracture is produced in peak aged alloy 2090 by both fatigue in water vapor (Figure 8a) and overload tensile fracture (Figure 8b). It is speculated that  $T_1$  precipitates, concentrated along subgrain boundaries (Figure 2c), enhance environmentally induced subgranular fatigue fracture; possibly by trapping atomic hydrogen. Hydrogen enhanced subgranular fatigue crack surfaces are smooth, with no evidence of the tearing or dimpling that is observed in the overload region. Intersubgranular overload fracture is probably produced in this alloy because the higher aging temperature concentrated  $T_1$  precipitates along subgrain boundaries, and is unrelated to hydrogen embrittlement. Shorter aging times or lower peak aging temperatures produce a microstructure that fails by slip band overload fracture, rather than the subboundary mode<sup>(44)</sup>. The corrosion fatigue behavior of these heat treatments is not characterized.

For constant low  $\Delta K$  levels of 3.0 MPa $\sqrt{m}$  and 1.5 MPa $\sqrt{m}$  at high  $K_{max}$ , the environmental fatigue crack surface exhibits a flat crystallographic morphology, regions 2 and 3 in Figure 7. The dashed line in Figure 7 and the dashed line in the high magnification fractograph in Figure 8c show the high  $\Delta K$  (intersubgranular at 16.2 MPa $\sqrt{m}$ ) to low  $\Delta K$  (faceted cracking at 3.1 and 1.5 MPa $\sqrt{m}$ ) morphology transition. Etch pit analysis of the low  $\Delta K$  crystallographic regions reveals a square pit geometry (identical to that shown in Figure 10c for aqueous NaCl), indicating that cracking is crystallographic along {100} planes.

Small areas of periodic, striation like markings (area D in Figure 8c) are observed on the crystallographic surface produced at a  $\Delta K$  of 3 MPa $\sqrt{m}$ . Examination at high magnification reveals brittle striations similar to "intermediate type" striations, identified by Nix and Flower

for Al-Zn-Mg-Cu fatigued in laboratory air<sup>(15)</sup>. Similar to their findings,  $\Delta a/\Delta N$ , calculated from the striation spacing and the assumption of per cycle crack advance, overestimates macroscopically measured  $da/dN$ . (For a  $\Delta K$  of 3 MPa $\sqrt{m}$ , the striation based  $\Delta a/\Delta N$  is  $10^{-3}$  mm/cycle, while the macroscopic  $da/dN$  for water vapor is  $3 \times 10^{-6}$  mm/cycle.) This result suggests that near-threshold environmental FCP is discontinuous, with on the order of 300 load cycles required for an increment of crack advance.

**2. Moist Air:** FCP in the alloy 2090-moist air system progresses by a combination of the morphologies produced by mechanical fatigue in the inert environment and hydrogen environment cracking observed for pure water vapor; that is, slip band cracking, subgrain boundary separation and {100} cracking. At high  $\Delta K$  ( $\geq 10$  MPa $\sqrt{m}$ ), 2090 exhibits severe planar deflections along {111} planes, as verified by etch pitting analysis, and coupled with SGC. Approximately 50% of the fatigue surface is intersubgranular and 50% is {111} SBC. The proportion of {111} cracking increases with  $\Delta K$ , and is present in significantly greater amounts than that observed for water vapor, but is less than that observed for the inert environments. Literature results have largely emphasized slip band cracking for 2090 in moist air<sup>(25,26,28,30,32-35)</sup>. Subgrain boundary fatigue cracking in moist air is likely to be by both hydrogen embrittlement (similar to water vapor, Figures 7 and 8) and by mechanical fracture (similar to the inert environments, Figure 4). Since the population of  $T_1$  at subgrain boundaries varies with aging conditions, heat treatment probably affects the proportions of SGC and SBC.

The fatigue crack surface shown in Figure 9 for low and intermediate cyclic stress intensities, 1.6 to 6.6 MPa $\sqrt{m}$ , is different than that observed for high  $\Delta K$  growth. Broad flat crystallographic areas are observed. Etch pit analysis of these regions reveals a {100} crack plane, similar to low  $\Delta K$  fatigue crack surfaces formed in pure water vapor. At an SEM resolution of better than 0.1  $\mu m$ , striations were not observed on moist air fatigue surfaces at any  $\Delta K$  level.

**3. Aqueous NaCl with Anodic Polarization:** FCP in the alloy 2090-aqueous NaCl (anodic polarization) system progresses by subgrain boundary and flat crystallographic cracking, similar to the water vapor and moist air cases. Figure 10a shows the fatigue surface for 2090 exposed to 1% NaCl at -840 mV. A distinct change in fracture mode is observed for the two regions of constant  $\Delta K$ . At high  $\Delta K$  (15.4 MPa $\sqrt{m}$ , Region 1), the fatigue crack grows primarily along subgrain boundaries, as shown at higher magnification in Figure 10b. The

subgranular area to the right of the dashed line exhibits two prominent features: subgrains protruding from the surface and secondary cracking along subgrain boundaries, as identified by the arrows. This surface exhibits some corrosion debris, but is generally free of large pits and corrosion product in spite of the applied anodic potential. Examination at higher magnification reveals little evidence of tearing plasticity or corrosion on subgrain surfaces, suggesting brittle crack growth. Small regions of {111} SBC are observed on the high  $\Delta K$  fracture surface, Figure 10a. The {111} regions are presumably not environmentally induced based on inert environment fractography, however, hydrogen can promote slip plane cracking<sup>(34,36)</sup>.

The dashed line in Figure 10b shows the change in fracture morphology for the step reduction in constant  $\Delta K$  (at Region A in Figure 10a). At low  $\Delta K$  (1.6 MPa $\sqrt{m}$ ), a flat faceted crack morphology is observed, similar to the moist gas environments. Low  $\Delta K$  cracking is along {100} planes, as verified by the square etch pits in Figure 10c. The low crack growth rate regions exhibit little evidence of localized corrosion and corrosion products, although examination at high magnification (Region C in Figure 10a) reveals small regions of localized corrosion on subgrain boundaries, Figure 10d. The features in Figure 10d are similar to those identified during corrosion testing (Figure 3b) and are due to  $T_1$  dissolution.

**4. Aqueous NaCl with Cathodic Polarization:** Fatigue fracture surfaces produced in aqueous NaCl with mild cathodic polarization exhibit a black surface film that was not observed for the anodic potential case. Figure 11 shows the fracture surface for alloy 2090 exposed to 1% NaCl at -1.240 mV. Note the thick surface deposit that is not observed for the anodic potential case represented in Figure 10. (The deposits appear white due to electron charging in the SEM.) The thick surface layer obscures the detail of the fatigue crack morphology. In general such surfaces exhibit a flat morphology with little evidence of tortuous SBC, suggesting subgrain boundary and crystallographic cracking similar to the other hydrogen producing environments. In fact, examination of near crack tip fracture surfaces, which contain minimal reaction products, revealed low  $\Delta K$  fatigue fracture along {100} planes.

## IV. DISCUSSION

### A. *Fracture Surface Morphology and Crack Growth Kinetics*

The fractographic analysis establishes several microscopic fatigue cracking mode transitions, but only for alloy 2090 in the hydrogen producing environments. Figure 12 correlates 2090 fatigue crack surface morphologies with  $da/dN$ - $\Delta K$  data from Part I<sup>(1)</sup>. One or

more of the possible fatigue damage modes; including mechanically induced slip band cracking along {111} planes (SBC), and environment promoted intersubgranular cracking (SGC) and crystallographic {100} cracking; operate depending on  $\Delta K$  and environment activity. High angle grain boundaries have no influence on L-T and L-S orientation FCP in alloy 2090<sup>(37)</sup>.

**1. Mechanical Fatigue:** In the absence of an environmental influence, highly tortuous transgranular slip band cracking is the primary fatigue cracking mode for textured peak aged alloy 2090 plate at all  $\Delta K$  levels. The correlation in Figure 12 reveals that intrinsic crack growth by SBC depends on  $\Delta K$  through a single power law, indicative of a single crack tip damage mechanism for FCP in vacuum, helium and oxygen. The surface oxide film that formed in oxygen had no resolvable effect on either  $da/dN$  or the SBC cracking morphology, contrary to proposed film effects on slip<sup>(5,25,45,46)</sup>.

While pronounced for peakaged and textured alloy 2090 plate, and reported for 8090 and 2091<sup>(34,35)</sup>, the generality of SBC for Al-Li-X in inert environments is unclear. Alloy composition (e.g., lower Li to copper ratio or incoherent particle formers such as Zr) and aging conditions (e.g., overaging or aging above the  $\delta'$  solvus) that reduce  $\delta'$  formation or promote nonshearable precipitates are likely to reduce slip localization and hinder SBC. Grain size, texture and specimen orientation determine the size and geometry of slip plane facets, and are likely to affect SBC. The inert environment mode that occurs in the absence of slip band cracking in Al-Li alloys has not been identified. Fundamental studies of fatigue damage in Al-Li-based alloys in vacuum/helium and oxygen environments must be conducted.

**2. Chemically Assisted Fatigue:** From Figure 12, those environments that produce atomic hydrogen enhance  $da/dN$  by subgrain boundary and {100} fatigue cracking in unrecrystallized peak aged alloy 2090. While hydrogen may enhance {111} slip plane cracking<sup>(36)</sup>, SBC was not an important cracking mode for alloy 2090 in the hydrogen producing environments. Fatigue cracking in these environments is probably less roughness-based closure affected compared to the inert environments because of reduced SBC and an increased incidence of "flat" intersubgranular and {100} cracking.

The intrinsic  $da/dN$ - $\Delta K$  transition points (labelled 1 (1') and 2 after Wanhill<sup>(9)</sup>) in Figure 12 approximately correlate with the observed fatigue cracking mode transitions<sup>5</sup>. Considering

---

<sup>5</sup>The identification of specific transition points is idealized. Rather,  $da/dN$  and the fatigue crack path are likely to continuously vary with  $\Delta K$  as discussed in Part III<sup>(3)</sup>.

FCP in moist air, slope changes occur at points 1 and 2, and form a transition or "plateau" regime<sup>(34,37)</sup>. For  $\Delta K$  greater than 7 to 10 MPa $\sqrt{m}$  (above point 2), the amounts of SBC and subgrain boundary cracking are comparable. Moist air  $da/dN$  values are only slightly greater than those observed for the inert environments in spite of the fact that intersubgranular fatigue cracking is not produced in the latter. At intermediate  $\Delta K$  between points 1 and 2, SBC is minimal and environmentally induced {100} cracking and subgrain boundary cracking are associated with accelerated fatigue crack growth rates. With decreasing  $\Delta K$  from 7 MPa $\sqrt{m}$  to 3 MPa $\sqrt{m}$ , there is a gradual transition from SGC to {100} cracking. For low  $\Delta K$ , below point 1 in Figure 12, the slope of the moist air FCP relationship changes and cracking is exclusively along {100} planes.

For FCP in aqueous chloride, slip band cracking is minimal at all  $\Delta K$  and SGC is the predominant mode above point 1'. The high  $\Delta K$  transition (type 2) is not observed, consistent with the lack of mechanically induced SBC. The transition from subboundary to {100} cracking occurs at a low  $\Delta K$  of 2.0 MPa $\sqrt{m}$  (1'), correlating with the type 1 transition for moist air; Figure 12. For FCP in NaCl, water vapor, and moist air, respectively, it is speculated that the trends of: (a) reduced  $da/dN$ , (b) decreasing SGC/increasing SBC, and (c) the increase in the  $\Delta K$  value at the type 1 transition are due to reduced crack tip hydrogen production and uptake efficiency.

The importance of cyclic deformation in environmental cracking is supported by the results in Figure 12. For each hydrogen producing environment, as  $\Delta K$  decreases with increasing R and constant  $K_{max}$ , the fatigue fracture mode changes from intersubgranular to {100} cracking. The crystallographic cracking mode is not typically characteristic of monotonic load cracking of aluminum and Al-Li alloys in aqueous NaCl<sup>(47,48)</sup>. FCP in water vapor and aqueous NaCl is not influenced by high angle grain boundaries, a known contributor to SCC<sup>(47,48)</sup>.

**3. Microstructure-Environment Interaction:** Fractographic results show that crack tip fatigue damage in alloy 2090 is governed by the interaction of environment, cyclic plasticity and microstructure. This interaction is more complex than the hypothesis that transitions in the power-law  $da/dN$ - $\Delta K$  relationship occur when the cyclic plastic zone size ( $d_{cpz}$ ) is less than the average distance (L) between microstructural barriers to slip<sup>(9,49,50)</sup>. Based on this model, the transition  $\Delta K$  level,  $\Delta K_T$ , is given by:  $\Delta K_T = 5.5\sigma_y\sqrt{L}$ <sup>(49,50)</sup>. Considering FCP in the 7475 and 2024-moist air, sump water and aqueous NaCl systems, Wanhill reported two transitions at near threshold  $\Delta K$  levels similar to points 1 and 2 in Figure 12. Based on approximate equalities

between estimated cyclic plastic zone sizes and mean microstructural distances, he ascribed transition 1 to slip blockage by dispersoids (0.6 to 1.0  $\mu\text{m}$  spacing) and transition 2 to fatigue induced dislocation cell barriers (0.6 to 1.8  $\mu\text{m}$ )<sup>(9)</sup>.<sup>6</sup> These calculations are compromised by uncertainties in the size and shape of the plastic zone. Critically, slip distance models imply that FCP rate transitions are solely mechanical; environmental effects are not explicitly considered in spite of the fact that the models are developed from and tested with  $da/dN$ -data obtained for the aggressive moist air environment.

The results in Figure 12 establish that  $da/dN$  transitions and crack path changes are not observed for FCP in inert environments (vacuum, He and  $\text{O}_2$ ), suggesting that microstructural barriers do not influence slip-based fatigue damage for the range of  $\Delta K$  studied. Stress intensity range only affects crack path and the  $da/dN$ - $\Delta K$  relationship in the presence of environmental hydrogen. While only proven for the Al-Li-Cu alloy, a similar explanation may be relevant to 2000 and 7000 series alloys. Crack tip damage may involve a critical microstructural distance for slip, however, hydrogen embrittlement must play an important role in the  $da/dN$ - $\Delta K$  relationship.

FCP rates, the shape of the  $da/dN$ - $\Delta K$  relationship and microscopic mode transitions are controlled by crack tip environment-microstructure interactions. Figure 13 schematically represents the FCP rate characteristics of peak aged alloy 2090, for inert and hydrogenous environments, and in conjunction with cyclic plastic zone size at any  $\Delta K$  and the range of subgrain sizes.<sup>7</sup> For simplicity, the crack tip damage process zone is equated to the cyclic plastic zone. As discussed in Part III, however, the process zone over which fatigue damage and crack extension occur is a fraction, albeit significant, of  $d_{cpz}$ <sup>(3)</sup>. Three regimes of behavior (A, B and C) are indicated based on the ratio of  $d_{cpz}$  to T-direction subgrain size. Subgrain size varied from 1 to 10  $\mu\text{m}$  in the T direction, with an average value of 5  $\mu\text{m}$ ; this subgrain size

---

<sup>6</sup>These alloys were recrystallized. When present, unrecrystallized subgrain boundaries decorated with precipitates should provide a barrier to slip<sup>(9)</sup>.

<sup>7</sup>It is only possible to estimate the diameter of the cyclic plastic zone,  $d_{cpz}$ . The value employed here is based on the Irwin/Rice estimate ( $d_{cpz} = [1/(12\pi)][\Delta K/\sigma_{ys}]^2$ ) for plane strain and assuming that the cyclic yield strength equals the monotonic value. This simple circular estimate of plastic zone size is reasonable<sup>(51)</sup>. Wanhill concludes that the coefficient varies from  $1/(71\pi)$  (direction within the crack plane) to  $1/(10\pi)$  (normal to the crack plane), depending on the location within the crack tip field and the difference between the monotonic and cyclic yield strengths<sup>(9)</sup>. Additional work is required to precisely define the true cyclic plastic zone size and shape for Al-Li alloys.

interval is plotted in Figure 13 on the  $d_{cpz}$  axis and is relevant to the growing L-T fatigue crack. The three regions of  $da/dN-\Delta K$  response are as follows.

**Region A:** When  $d_{cpz}$  is smaller than the smallest subgrain diameter ( $1 \mu\text{m}$ ),  $\{100\}$  cracking is dominant and the  $da/dN-\Delta K$  responses in moist air, water vapor and NaCl exhibit a similar high slope. This region of cracking corresponds to FCP below point 1 for moist air and 1' for NaCl, and therefore depends on hydrogen environment activity.

**Region B:** When  $d_{cpz}$  approaches the size of the subgrains (1 to  $10 \mu\text{m}$ ), FCP involves a substantial proportion of intersubgranular cracking that increases with increasing  $\Delta K$  and  $d_{cpz}$ . The amount of  $\{100\}$  cracking proportionately declines to zero and some mechanical  $\{111\}$  occurs at higher  $\Delta K$  levels. Plateau behavior, between points 1 and 2, occurs in Region B.

**Region C:** At high  $\Delta K$ , where  $d_{cpz}$  is larger than the average subgrain size of  $5 \mu\text{m}$ , FCP involves a significant proportion of  $\{111\}$  cracking. Here, a slope change is observed at point 2 and crack growth rates in water vapor and moist air approach levels for the inert environments.

### **B. Evidence of Hydrogen Embrittlement and the Role of Cyclic Deformation**

The results summarized in Figure 12 establish that fatigue cracking along  $\{100\}$  planes and subgrain boundaries is environmentally induced and not the result of purely mechanical mechanisms involving restricted-slip, alternate shear or localized slip<sup>(5,8,18)</sup>. For the cases where mechanical  $\{100\}$  cracking in precipitation hardened aluminum alloys is claimed, environment purity may not have been sufficiently controlled; part-per-million level water vapor contamination can produce hydrogen embrittlement of aluminum alloys<sup>(1,37)</sup>. For the current study, vacuum, helium and oxygen environments were highly purified and  $\{100\}$  cracking was never observed<sup>(1,37,39)</sup>.

The crack growth results presented in Part I<sup>(1)</sup> and fractographic observations summarized in Figure 12 strongly suggest a hydrogen embrittlement mechanism for environmental FCP in Al-Li-Cu alloys. Identical slow FCP rates in pure oxygen, inert helium and vacuum establish that oxygen, and by inference surface films, are not damaging. By elimination, fatigue crack growth rates in pure water vapor and moist air are accelerated by hydrogen produced from the reaction of adsorbed  $\text{H}_2\text{O}$  with newly created crack tip surfaces.  $Da/dN$  in low pressure water

vapor (0.01 Pa to 1 kPa) is not likely to be accelerated by capillary condensation and dissolution<sup>(1,37)</sup>. Condensation pressures, while reduced due to crack tip curvature, are several orders of magnitude larger than the water vapor levels which enhance  $da/dN$ .<sup>8</sup> Even if thermodynamically possible at low stress intensities or at a microstructurally sharper crack tip, the kinetics of water condensation are unclear and may be slow during a 5 Hz load cycle. The nature of any electrolyte formed by water condensation has not been specified.

Identical intersubgranular and {100} fatigue cracking modes are observed for moist air, water vapor and aqueous NaCl, indicating similar crack tip embrittlement mechanisms. For the NaCl electrolyte, hydrogen is cathodically evolved and absorbed for each applied electrode potential examined<sup>(2)</sup>. The correlation of fracture mode with  $\Delta K$ , cyclic plastic zone size and microstructure indicates that accelerated FCP in hydrogen environments is associated with an embrittled volume ahead of the crack tip and not surface film formation, rupture and anodic dissolution. Process zone volume embrittlement is consistent with crack tip hydrogen uptake and embrittlement. Crystallographic and grain boundary cracking are typical of hydrogen embrittlement<sup>(2,52)</sup>. Cracking along {100} planes in aqueous NaCl exhibits no evidence of precipitate dissolution and there is no clear description as to how electrochemical dissolution can produce brittle cracking along a crystallographic plane.

The atomistic mechanisms by which crack tip process zone hydrogen promotes both intersubgranular and {100} cracking are unclear; speculative explanations are developed in Part III<sup>(3)</sup>. Subgrain boundaries may be active cracking sites because of the presence of  $T_1$  precipitates which may act as strong hydrogen trap sites and which may stimulate local anodic dissolution that in turn enhances hydrogen production on adjacent cathodic sites. Crystallographic {100} cracking may be related to an aluminum-lithium hydride phase or to lattice decohesion. Hydrides were not observed during fractographic analyses of environmental fatigue crack surfaces of alloy 2090.

---

<sup>8</sup>Calculations based on the Kelvin equation indicate that condensation only occurs above  $0.01 P_0$  (where  $P_0$  is the water vapor pressure in equilibrium with the liquid on a plane surface; 3.2 kPa at 300 K) for a stress intensity of  $7 \text{ MPa}\sqrt{\text{m}}$  corresponding to a continuum crack tip radius of  $0.3 \mu\text{m}$ <sup>(37)</sup>.

## V. CONCLUSIONS

1. Intrinsic rates of fatigue crack propagation (FCP) in peak aged Al-Li-Cu alloy 2090 are accelerated by aqueous NaCl and water-bearing gaseous environments for the stress intensity regime where monotonic load environmental cracking does not occur.
2.  $\Delta K$  uniquely governs the degree of the environmental effect on  $da/dN$  and the microscopic crack path for constant high  $K_{max}$  cyclic loading, establishing the central importance of the crack tip cyclic process zone volume, consistent with hydrogen embrittlement but not surface film rupture and dissolution.
3. Both unrecrystallized subgrain boundaries with  $T_1$  precipitates and  $\{100\}$  planes are preferred paths for environmental FCP in alloy 2090, consistent with hydrogen embrittlement. High angle grain boundaries do not affect L-S and L-T orientation cracking.  $\{111\}$  slip plane cracking is the dominant damage mode for FCP in inert environments.
4. The fatigue crack path depends on stress intensity range and environment. For hydrogen producing environments (moist air, pure water vapor and NaCl), the path transitions from along subgrain boundaries to  $\{100\}$  planes as  $\Delta K$  decreases from moderate Paris regime to near-threshold levels. For inert helium or vacuum at all  $\Delta K$ , or when hydrogen environmental effects are minimal at high  $\Delta K$ , FCP is along slip planes due to precipitate induced slip localization. Slip plane cracking is dominant for FCP in pure oxygen at all  $\Delta K$  levels, analogous to the inert environments; surface oxide has no effect on either  $da/dN$  or the microscopic FCP mode.
5. Complex, multi-sloped  $\log da/dN$ - $\log \Delta K$  behavior is solely due to hydrogen environment embrittlement; changes in intrinsic  $da/dN$ - $\Delta K$  slope result from the interaction of the embrittled crack tip process zone (a significant fraction of the cyclic plastic zone) with microstructure.  $\{100\}$  cracking dominates when the process zone is substantially smaller than the subgrain size, while intersubgranular cracking occurs when the plastic zone encompasses one or more subgrains. The ratio of cyclic plastic zone size to

microstructural distance has no effect on the  $da/dN-\Delta K$  relationship for alloy 2090 in inert environments, casting doubt on micromechanical-microstructural critical distance based FCP models.

## VI. ACKNOWLEDGEMENTS

This research was supported by the NASA-Langley Research Center under Grant NAG-1-745, with D.L. Dicus as program monitor, and by the Virginia CIT Center for Electrochemical Science and Engineering at the University of Virginia. Alloy 2090 and texture analyses were provided by the Alcoa Technical Center. W.A. Cassada, R. Bayles, J.A. Wert, G.E. Stoner, E.A. Starke, J.C. Newman, Sang-Shik Kim and M.F. Henry provided important inputs to this work. These contributions are gratefully acknowledged.

## VII. REFERENCES

1. R.S. Piascik and R.P. Gangloff, Metall. Trans. A, Vol. 22A, pp. 2415-2428 (1990).
2. R.P. Gangloff, Environment Induced Cracking of Metals, R.P. Gangloff and M. Ives, eds., NACE, Houston, TX, pp. 55-109 (1990).
3. R.S. Piascik and R.P. Gangloff, "Environmental Fatigue of an Al-Li-Cu Alloy: Part III- Modeling of Crack Tip Hydrogen Damage, NASA TM-107619 (1992).
4. M. Gao, P.S. Pao and R.P. Wei, Metall. Trans. A, Vol. 19A, pp. 1739-1750 (1988).
5. R.M. Pelloux, Trans. ASM, Vol. 62, pp. 281-284 (1969).
6. C. Laird, Fatigue Crack Propagation, ASTM STP 415, ASTM, Philadelphia, PA, pp. 131-168 (1967).
7. P.J.E. Forsyth and D.A. Ryder, Metallurgia, Vol. 63, pp. 117-124 (1961).
8. E.A. Starke, Jr., and G. Luterig, Fatigue and Microstructure, ASM, Metals Park, OH, pp. 205-243 (1979).
9. R.J.H. Wanhill and L. Schra, "Corrosion Fatigue Crack Arrest in Aluminum Alloys", NLR Report NLR TR 87128 U, National Aerospace Laboratory, Amsterdam, Netherlands (1987).
10. J.A. Feeney, J.C. McMillan and R.P. Wei, Met. Trans., Vol. 1, pp. 1741-1757 (1970).
11. D.A. Meyn, Met. Trans., Vol. 2, pp. 853-865 (1971).
12. P.J.E. Forsyth, Acta Metall., Vol. 11, pp. 703-716 (1963).
13. C.A. Stubbington, Metallurgia, Vol. 65, pp. 109-121 (1963).
14. N.J.H. Holroyd and D. Hardie, Corrosion Science, Vol. 23, pp. 527-546 (1983).
15. K.J. Nix and H.M. Flower, Acta Metall., Vol. 23, pp. 841-848 (1975).
16. J. Lankford and D.L. Davidson, Acta Metall., Vol. 31, pp. 1273-1284 (1982).
17. R.E. Stoltz and R.M. Pelloux, Metall. Trans., Vol. 3, pp. 2433-2441 (1972).
18. G.G. Garrett and J.F. Knott, Acta Metall., Vol. 23, pp. 841-848 (1975).

19. P.E. Bretz, B.J. Bucci, P.C. Malcolm and A.K. Vasudevan, Fracture Mechanics: Fourteenth Symposium, Vol. I, ASTM STP-791, ASTM, Philadelphia, PA, pp. 67-86 (1983).
20. P.J.E. Forsyth, C.A. Stubbington and D. Clark, J. Inst. Metals, Vol. 90, pp. 238-247 (1962).
21. A. Niegel, H.-J. Gudladt and V. Gerold, Fatigue '87, R.O. Ritchie and E.A. Starke, Jr., eds., EMAS, West Midlands, UK, pp. 1229-1238 (1987).
22. A. Niegel, H.-J. Gudladt and V. Gerold, J. de Physique, Colloque C5, Vol. 49, pp. 659-663 (1988).
23. F.P. Ford, Corrosion, Vol. 35, pp. 281-287 (1979).
24. F.P. Ford, Environment Induced Cracking of Metals, R.P. Gangloff and M. Ives, eds., NACE, Houston, TX, pp. 139-165 (1990).
25. K.V. Jata and E.A. Starke, Jr., Metall. Trans. A, Vol. 17A, pp. 1011-1026 (1986).
26. K.T. Venkateswara Rao and R.O. Ritchie, "Fatigue of Aluminum-Lithium Alloys", University of California, Report No. LBL-30176, Berkeley, CA (1991).
27. J.M. Duva, M.A. Daeubler, E.A. Starke, Jr. and G. Luetjering, Acta Metall., Vol. 36, pp. 585-589 (1987).
28. G.R. Yoder, P.S. Pao, M.A. Imam and L.A. Cooley, Advances in Fracture Research, K. Salama, K. Ravi-Chandar, D.M.R. Taplin and P. Rama Rao, eds., Pergamon, Oxford, UK, pp. 919-927 (1989).
29. K.T. Venkateswara Rao, W. Yu and R.O. Ritchie, Metall. Trans. A, Vol. 19A, pp. 549-561 and pp. 563-569 (1988).
30. G.R. Yoder, P.S. Pao, M.A. Imam and L.A. Cooley, Aluminum-Lithium 5, T.A. Sanders, Jr. and E.A. Starke, eds., Jr., MCEP Ltd., Birmingham, UK, pp. 1033-1041 (1989).
31. P.S. Pao, M.A. Imam, L.A. Cooley and G.R. Yoder, Corrosion, Vol. 45, pp. 530-535 (1989).
32. M. Peters, V. Bachmann and K. Welpmann, Journal de Physique, Colloque C3, Supplement 9, pp. C3-785-791 (1987).
33. T. Magnin, P. Rieux, C. Lespinasse and C. Bathias, Journal de Physique, Colloque C3, Supplement 9, pp. C3-817-822 (1987).
34. N. Ohrloff, A. Gysler and G. Luetjering, Journal de Physique, Colloque C3, Supplement 9, pp. C3-801-807 (1987).
35. R. Tintillier, H.S. Yang, N. Ranganathan and J. Petit, Journal de Physique, Colloque C3, Supplement 9, pp. C3-777-784 (1987).
36. G.S. Chen and D.J. Duquette, "The Effect of Ageing on the Hydrogen-Assisted Fatigue Cracking of a Precipitation Hardened Al-Li-Zr Alloy", PhD Dissertation, Rensselaer Polytechnic Institute, Troy, NY (1991).
37. R.S. Piascik, "Mechanisms of Intrinsic Damage Localization During Corrosion Fatigue: Al-Li-Cu System", PhD Dissertation, University of Virginia, Charlottesville, VA (1990).
38. M.H. Tosten, A.K. Vasudevan and P.R. Howell, Aluminum - Lithium Alloys III, C. Barker, P.J. Gregson, S.J. Harris and C.J. Peel, eds., Institute of Metals, Oxford, UK, pp. 490-495 (1986).

39. R.S. Piascik and R.P. Gangloff, Environmental Cracking of Metals, R.P. Gangloff and M.B. Ives, eds., NACE, Houston, TX, pp. 233-240 (1990).
40. Chuang-Hsi Tracy Tsao and P.P. Pizzo, "A Potentiodynamic Study of Aluminum Lithium: Alloys in Aqueous Sodium Chloride Environment", Corrosion 85, Paper No. 53, NACE, Houston, TX (1985).
41. R.G. Buchheit, Jr., and G.E. Stoner, Aluminum-Lithium Alloys, T.H. Sanders, Jr., and E.A. Starke, Jr., eds., MCEP Led., Birmingham, UK, pp. 1347-1356 (1989).
42. R.G. Buchheit, Jr., J.P. Moran and G.E. Stoner, Corrosion, Vol. 46, pp. 610-617 (1990).
43. S. Suresh, Metall. Trans. A, Vol. 14A, pp. 2375-2385 (1983).
44. K.T. Venkateswara Rao, W. Yu and R.O. Ritchie, Metall. Trans. A, Vol. 20A, pp. 485-497 (1989).
45. N.M. Grinberg, Intl. J. Fatigue, pp. 83-95, April (1982).
46. H.L. Marcus, J.C. Williams and N.E. Paton, Corrosion Fatigue: Chemistry, Mechanics and Microstructure, NACE-1, O. Devereux, A.J. McEvily, and R.W. Staehle, eds., NACE, Houston, TX, pp. 346-358 (1972).
47. N.J.H. Holroyd, Environment Induced Cracking of Metals, R.P. Gangloff and M. Ives, eds., NACE, Houston, TX, pp. 311-345 (1990).
48. R.C. Dorwood and K.R. Hasse, Corrosion, Vol. 44, No. 12, pp. 932-941 (1988).
49. G.R. Yoder, L.A. Cooley and T.W. Crooker, Fracture Mechanics: Fourteenth Symposium ASTM STP 791, Vol. 1, J.C. Lewis and G. Sines, eds., ASTM, Philadelphia, PA, pp. 313-349 (1983).
50. G.R. Yoder, L.A. Cooley and T.W. Crooker, Scripta Metall., Vol. 16, pp. 1021-1025 (1982).
51. W.W. Gerberich and S. Chen, Environmental Induced Cracking of Metals, R.P. Gangloff and M.B. Ives, eds., NACE, Houston, TX, pp. 167-187 (1990).
52. H.K. Birnbaum, Environment Induced Cracking of Metals, R.P. Gangloff and M. Ives, eds., NACE, Houston, TX, pp. 21-29 (1990).

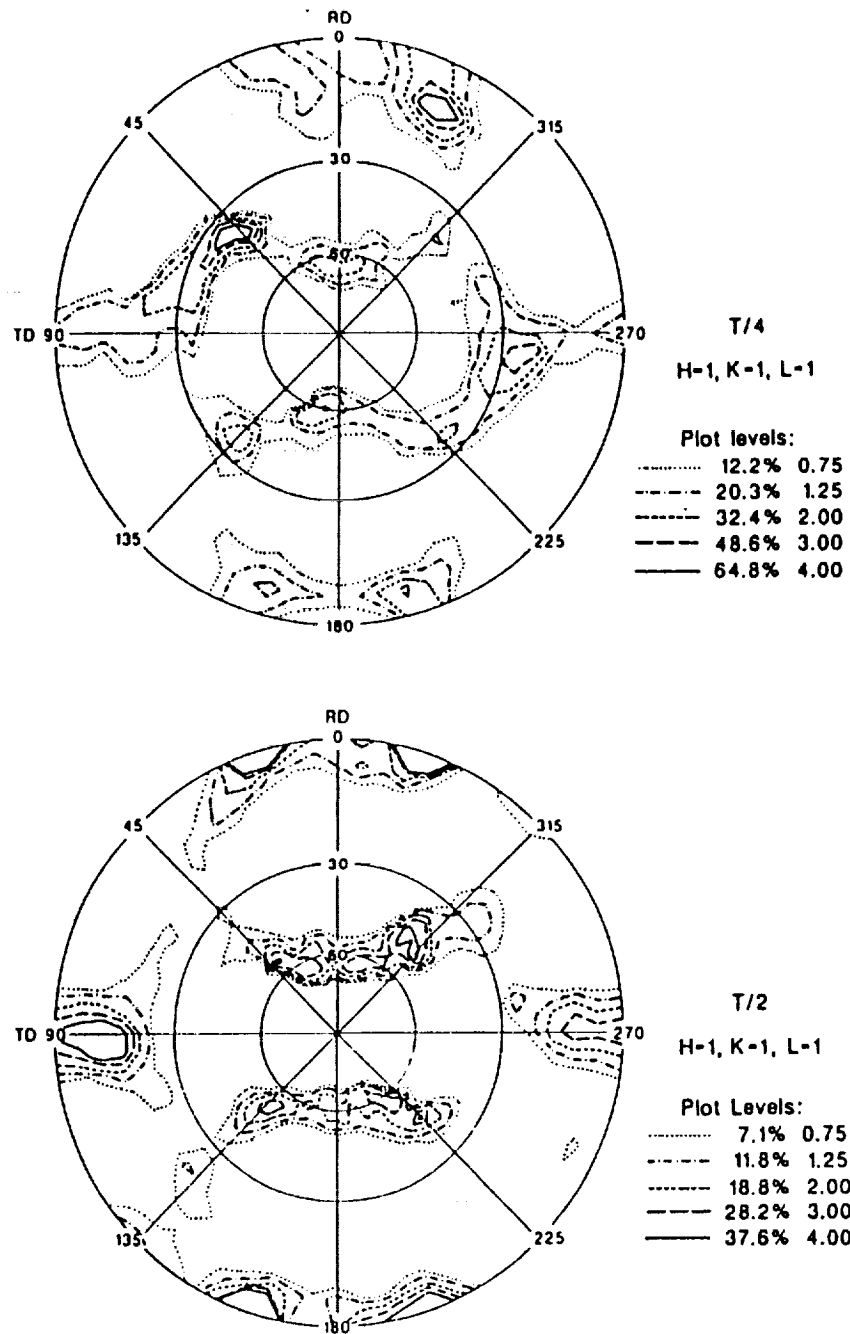


*Figure 1* Crystallographic texture of 2090 represented by {111} pole figures at two plate locations; (a) T/4 thickness and (b) T/2 thickness. (RD = rolling direction (longitudinal); TD = transverse direction.)

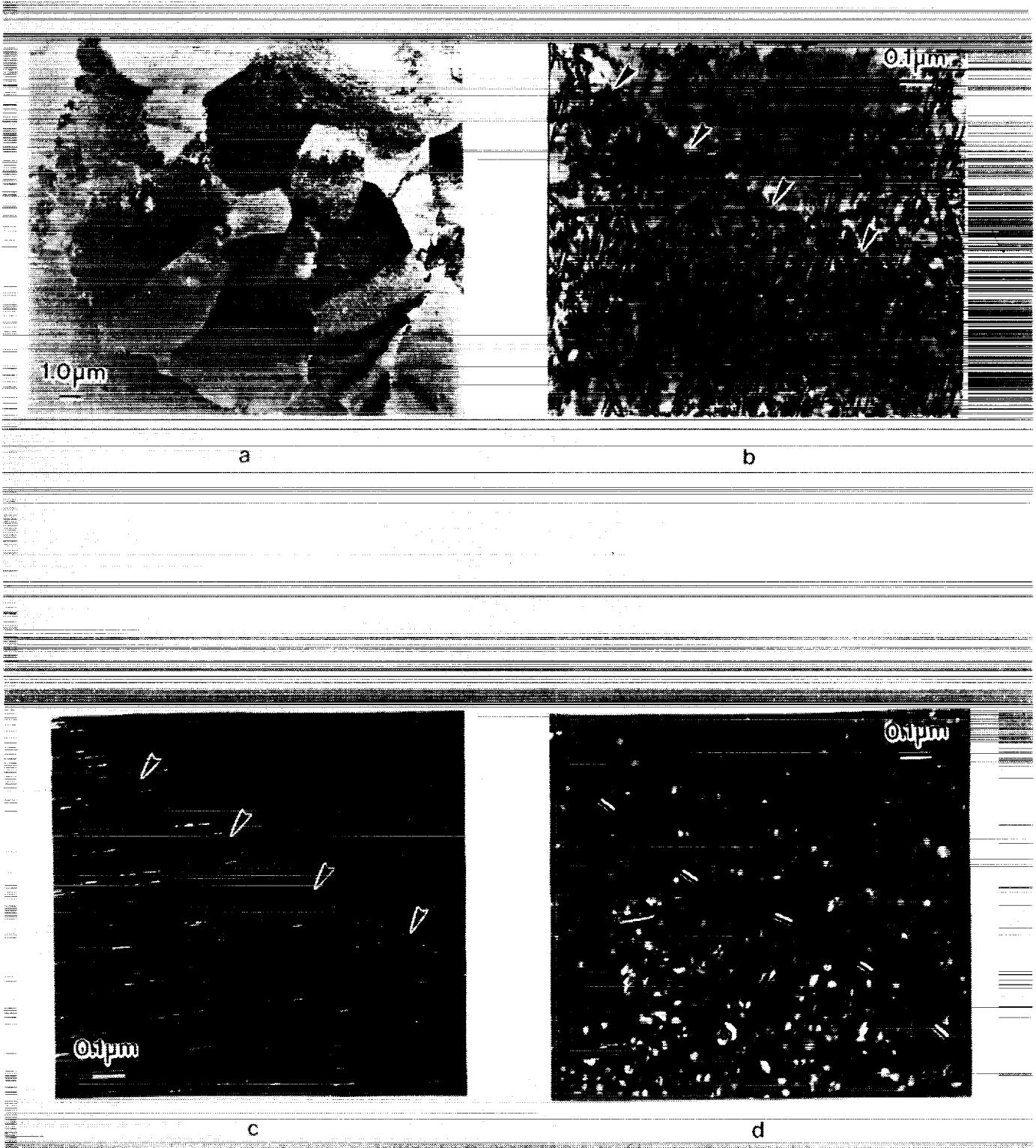
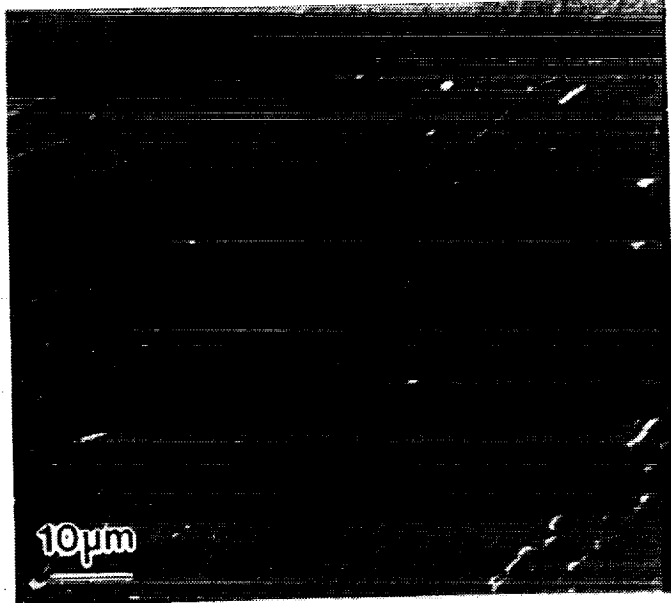
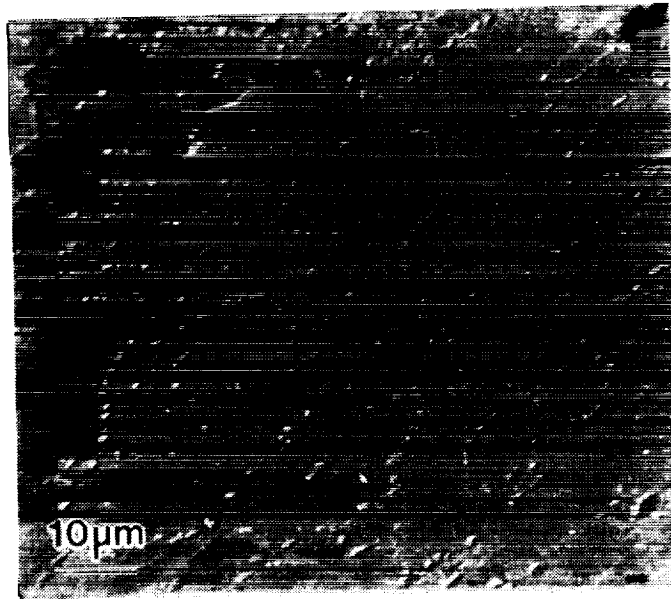


**Figure 2** Transmission electron micrographs of peak aged 2090. (a) Bright field micrograph of unrecrystallized subgrains; (b), (c) and (d) precipitate morphologies near subgrain boundaries. (b) BF micrograph,  $g = (112)$ ; (c)  $T_1$ -centered dark field of the grain boundary in "b",  $g = (0002)$ ; (d)  $\delta'$  centered DF of the subgrain boundary area in "b",  $g = 2/3(220)$ .



a



b

**Figure 3** Subgrain boundary pitting in peak aged alloy 2090; (a) etched (Keller's reagent) subgrains, (b) unetched and exposed to deaerated 0.1% NaCl for 3.5 days at  $-1000 \text{ mV}_{\text{SCE}}$ .



**Figure 4** (a) Fatigue fracture surface of peak aged alloy 2090, L-T orientation, exposed to helium containing ppm levels of  $H_2O$  ( $0^\circ$  tilt). Regions of constant  $\Delta K$  at 5 Hz are shown; (1)  $10.6 \text{ MPa}\sqrt{\text{m}}$  ( $R = 0.05$ ), (2)  $16.2 \text{ MPa}\sqrt{\text{m}}$  ( $R = 0.05$ ) and (3)  $2.4 \text{ MPa}\sqrt{\text{m}}$  ( $R = 0.86$ ). (b) Metallographic section of region A-A in "a", etched using Keller's reagent. Apparent grain boundaries are noted by arrows.

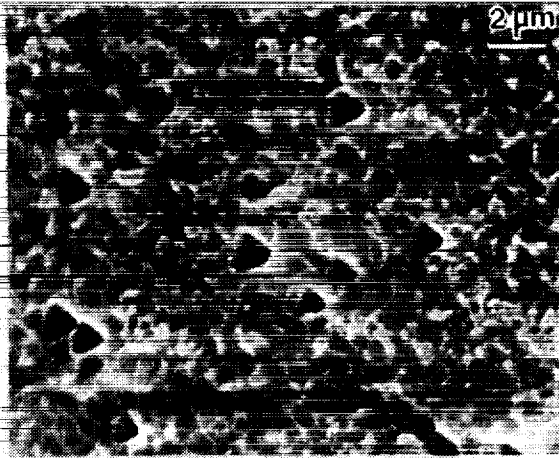


**Figure 5** SEM micrograph showing the etched crack surface of peak aged alloy 2090 (L-T) fatigue loaded in vacuum at  $\Delta K = 5 \text{ MPa}\sqrt{\text{m}}$  (5 Hz,  $R = 0.7$ ). The triangular pits indicate  $\{111\}$  slip plane cracking.

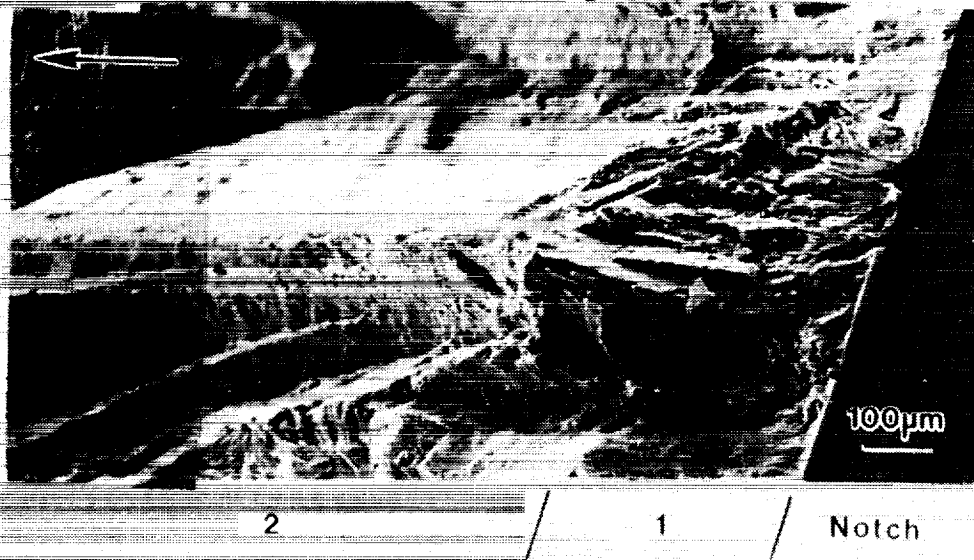


**Figure 6** SEM fractograph of the fatigue fracture surface of peak aged alloy 2090 (L-T) exposed to oxygen at  $f = 5 \text{ Hz}$ . Regions of constant  $\Delta K$  are shown; (1)  $10.6 \text{ MPa}\sqrt{\text{m}}$  ( $R = 0.05$ ) and (2)  $16.2 \text{ MPa}\sqrt{\text{m}}$  ( $R=0.05$ ).

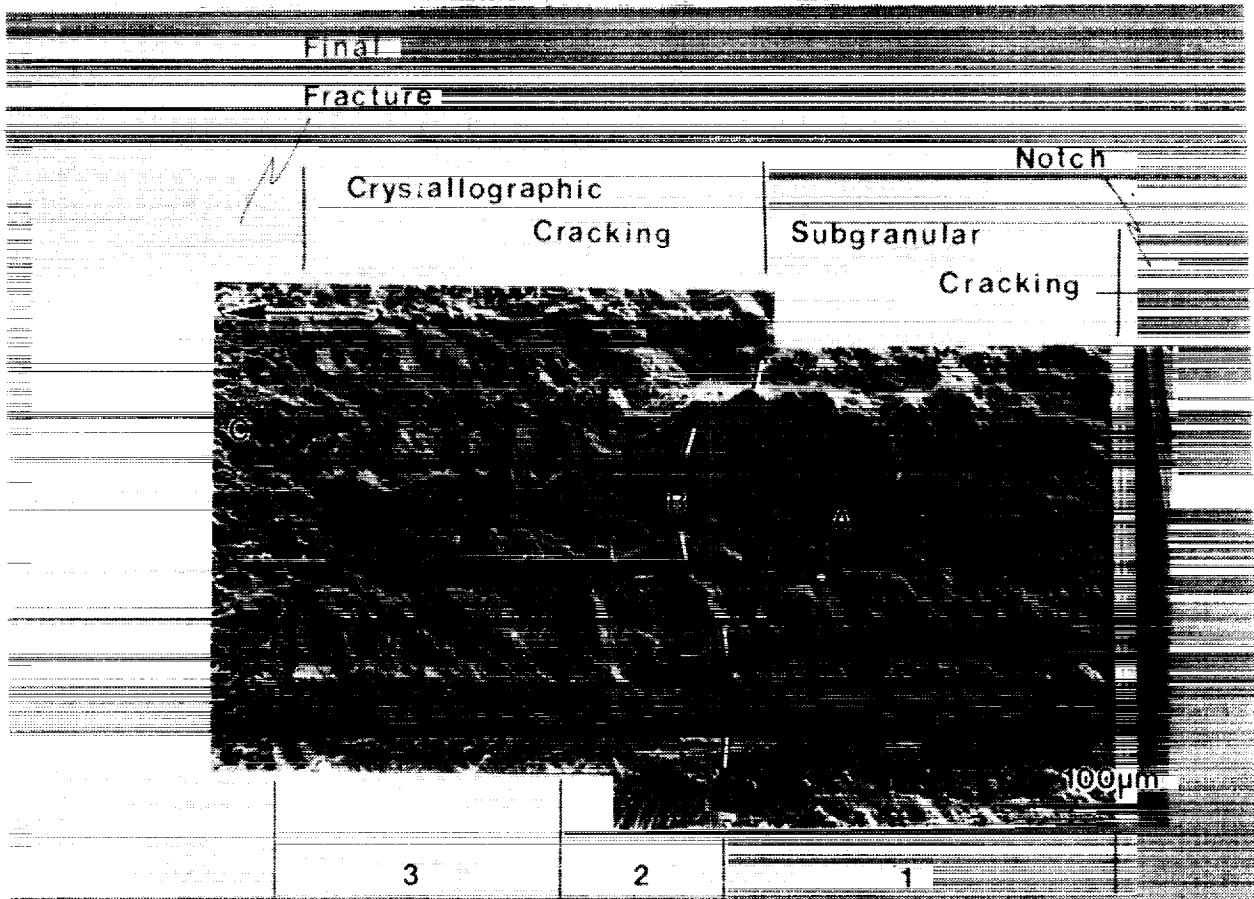
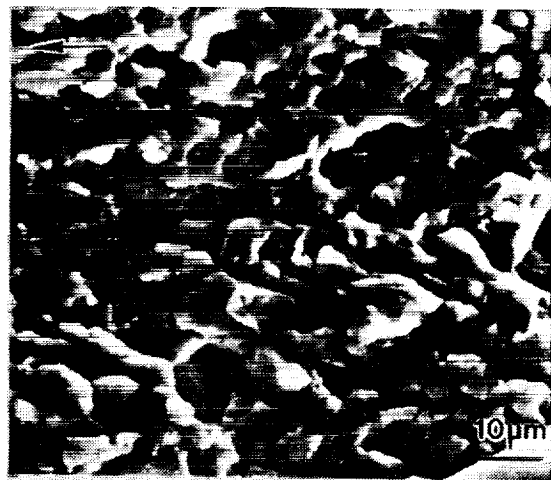
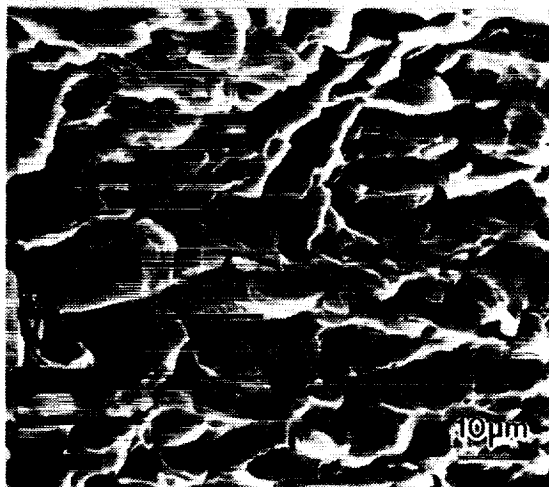


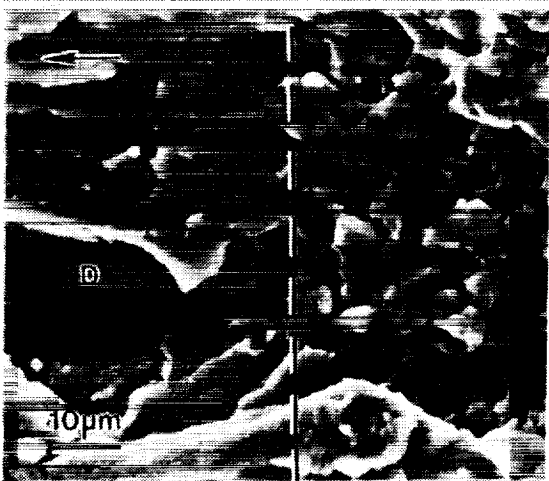
Figure 7 SEM fractograph of the fatigue crack surface of peak aged alloy 2090 (L-T) exposed to water vapor at  $f = 5$  Hz. Regions of constant  $\Delta K$  are shown; (1)  $16.2 \text{ MPa}\sqrt{\text{m}}$  ( $R = 0.05$ ), (2)  $3.1 \text{ MPa}\sqrt{\text{m}}$  ( $R = 0.82$ ) and (3)  $1.5 \text{ MPa}\sqrt{\text{m}}$  ( $R = 0.91$ ).



a



b



c

2

1

**Figure 8**

SEM fractographs showing detailed regions identified in Figure 7. (a) Region A; intersubgranular fatigue cracking in peak aged alloy 2090 (L-T) exposed to water vapor at  $16.2 \text{ MPa}\sqrt{\text{m}}$  ( $R = 0.05$ ), (b) Region C; SGC morphology of the monotonic overload fracture and (c) Region B; SGC to  $\{100\}$  cracking transition.

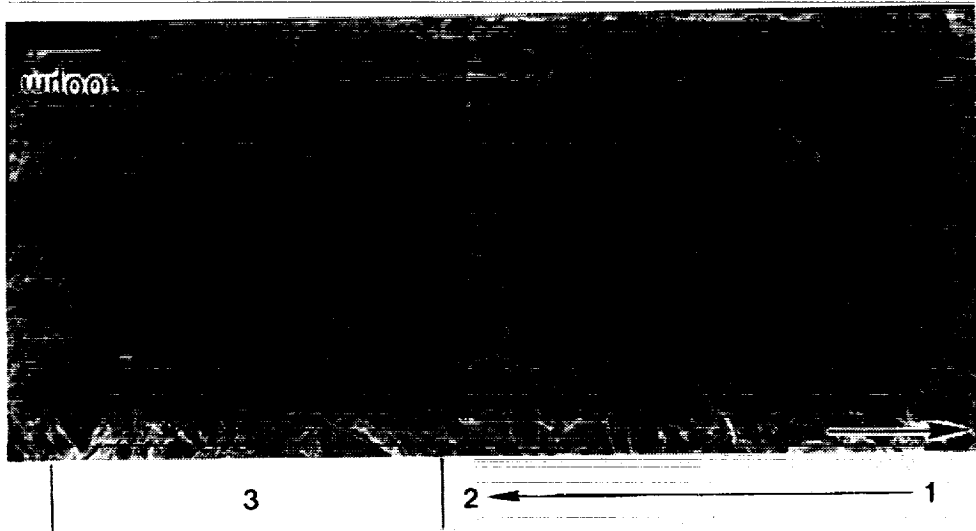


**Figure 9** SEM fractograph showing crystallographic {100} fatigue cracking in the 2090/moist air system for low  $\Delta K$  (1.6 to 3.3  $\text{MPa}\sqrt{\text{m}}$ ) Regions (1) and (2), and moderate  $\Delta K$  (6.0  $\text{MPa}\sqrt{\text{m}}$ ) Region (3).

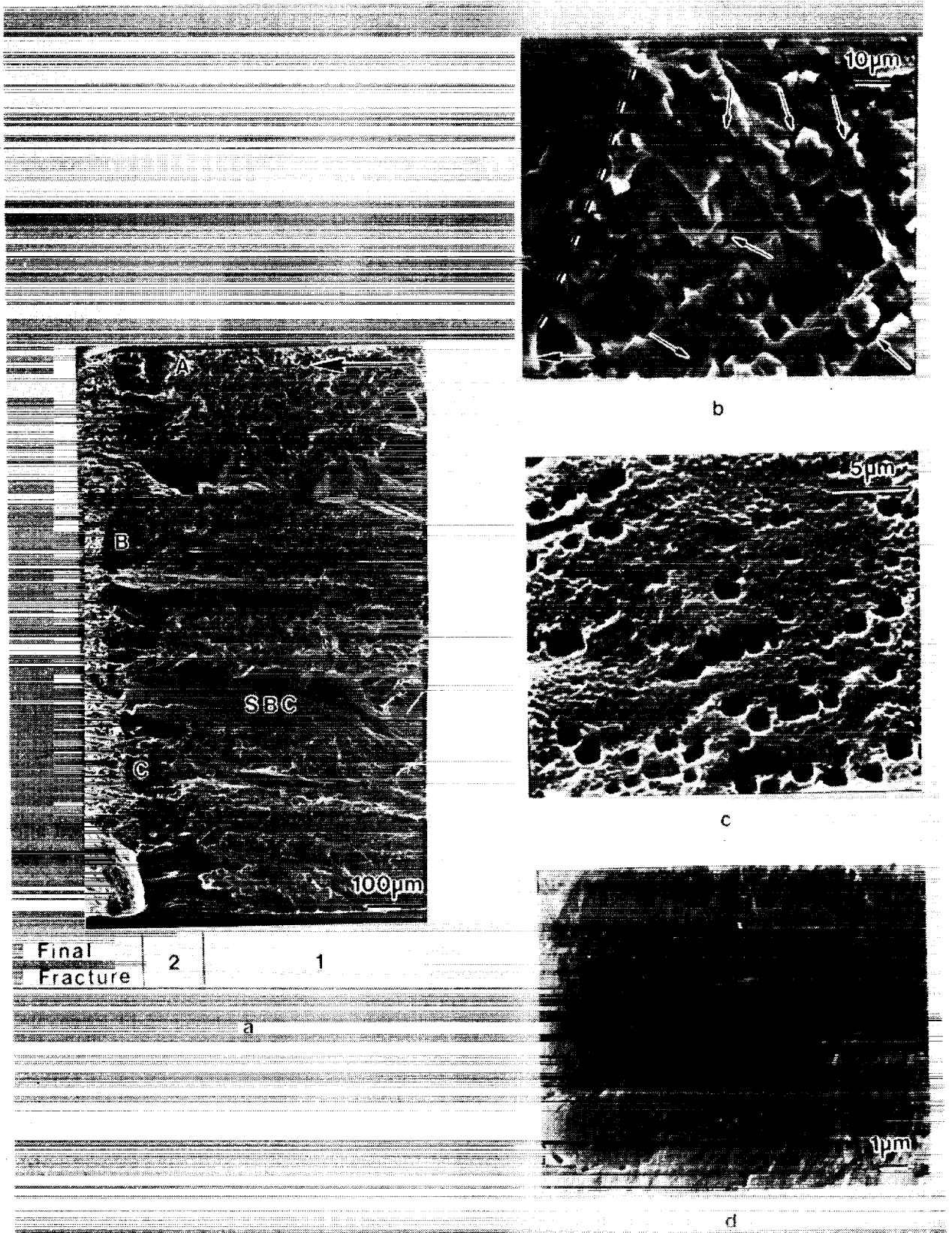
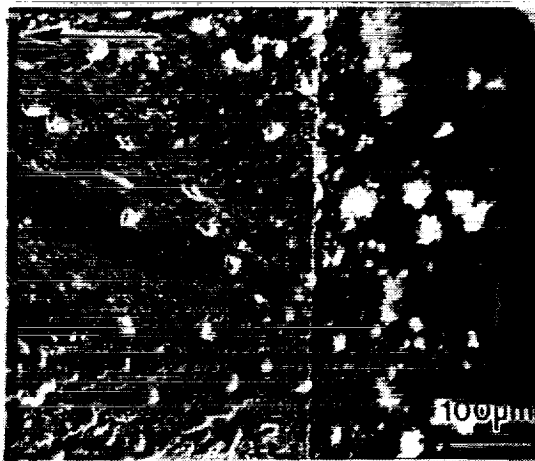


**Figure 10** (a) SEM fractograph of the fatigue crack surface in peak aged alloy 2090 (L-T) exposed to deaerated 1% NaCl ( $-840 \text{ mV}_{\text{SCE}}$ ) at 5 Hz. Regions of constant  $\Delta K$  are shown; (1)  $15.4 \text{ MPa}\sqrt{\text{m}}$  ( $R = 0.05$ ), (2)  $1.7 \text{ MPa}\sqrt{\text{m}}$  ( $R = 0.90$ ). (b) Dashed line divides the transition from SGC (right) at high  $\Delta K$  and  $\{100\}$  cracking (left) at low  $\Delta K$ . (c) Etched crystallographic fracture surface in Region B; the square pit geometry identifies the  $\{100\}$  fracture plane. (d) Crystallographic  $\{100\}$  fracture near the crack tip showing localized corrosion along subgrain boundaries in Region C.



Notch

**Figure 11** SEM fractograph of the film on the fatigue fracture surface of peak aged alloy 2090 (L-T) exposed to deaerated 1% NaCl at  $-1.240 \text{ mV}_{\text{SCE}}$ . ( $\Delta K = 10.4 \text{ MPa}\sqrt{\text{m}}$ ,  $R = 0.05$ ).

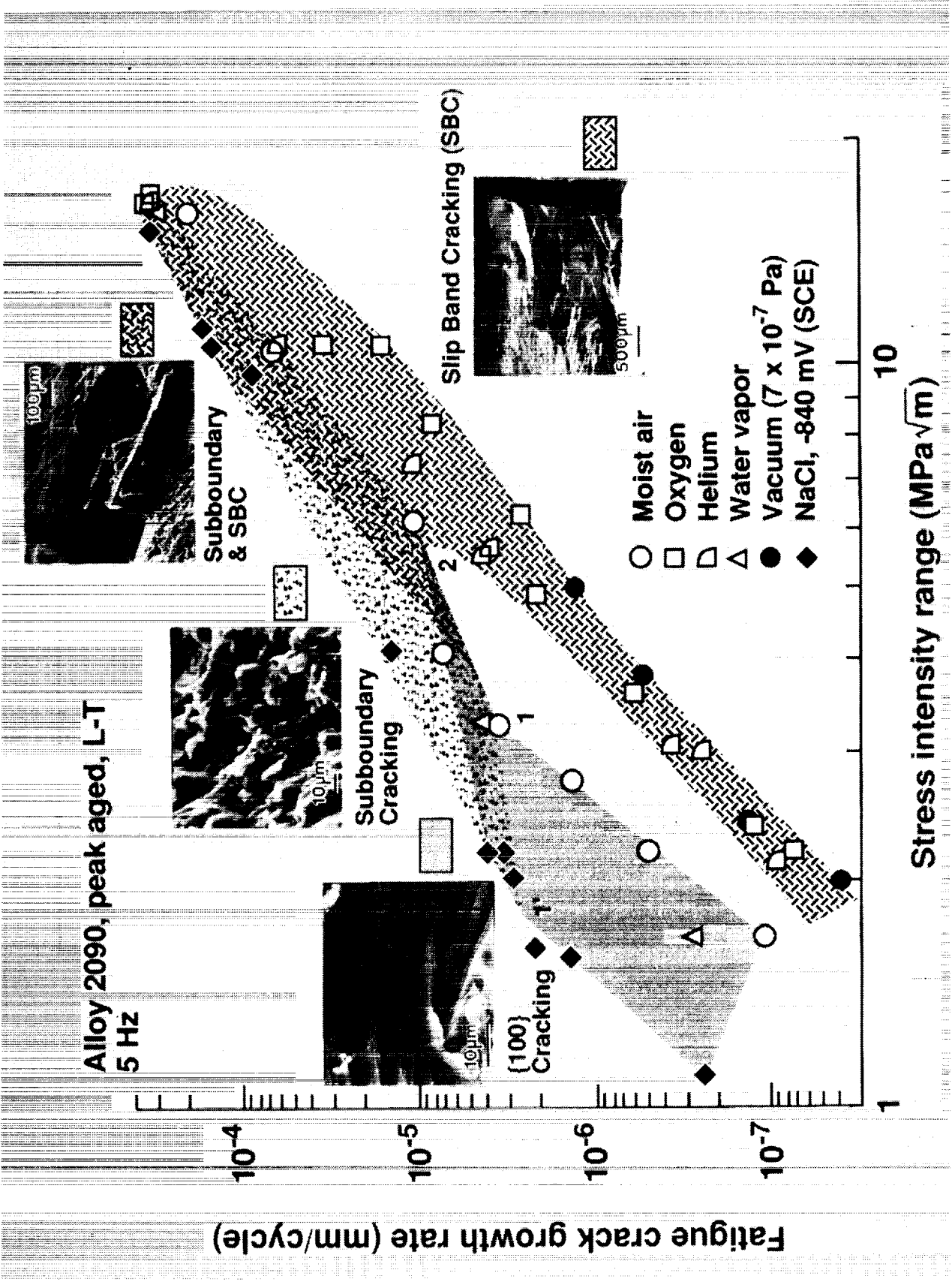
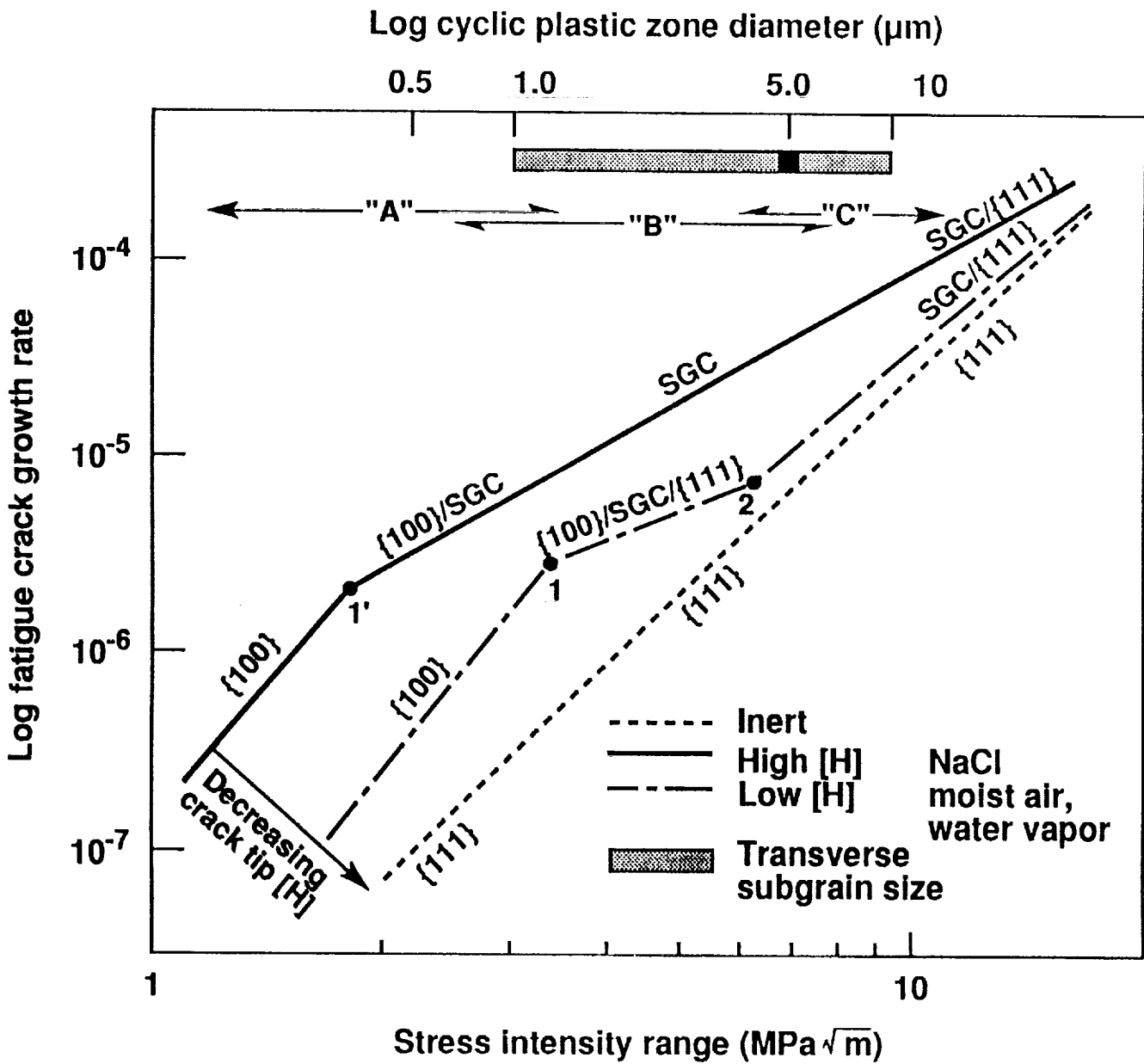


Figure 12 A correlation of peak aged alloy 2090 (L-T) fatigue crack growth kinetics from Part I<sup>(1)</sup>, and microscopic fracture paths for inert environments (vacuum, helium, and oxygen) and hydrogen producing environments (water vapor, moist air and aqueous NaCl) at constant  $K_{max}$ .



**Figure 13** A schematic of the effects of subgrain size and crack tip hydrogen concentration, [H], on the FCG characteristics of alloy 2090. (High [H] corresponds to anodic NaCl and low [H] to moist air.)

# REPORT DOCUMENTATION PAGE

Form Approved  
OMB No. 0704-0188

Public reporting burden for this collection of information is estimated to average 1 hour per response, including the time for reviewing instructions, searching existing data sources, gathering and maintaining the data needed, and completing and reviewing the collection of information. Send comments regarding this burden estimate or any other aspect of this collection of information, including suggestions for reducing this burden, to Washington Headquarters Services, Directorate for Information Operations and Reports, 1215 Jefferson Davis Highway, Suite 1204, Arlington, VA 22202-4302, and to the Office of Management and Budget, Paperwork Reduction Project (0704-0188), Washington, DC 20503.

<b>1. AGENCY USE ONLY (Leave blank)</b>	<b>2. REPORT DATE</b> May 1992	<b>3. REPORT TYPE AND DATES COVERED</b> Technical Memorandum	
<b>4. TITLE AND SUBTITLE</b> Environmental Fatigue of an Al-Li-Cu Alloy: Part II - Microscopic Hydrogen Cracking Processes		<b>5. FUNDING NUMBERS</b>  505-63-50-04	
<b>6. AUTHOR(S)</b> Robert S. Piascik and Richard P. Gangloff			
<b>7. PERFORMING ORGANIZATION NAME(S) AND ADDRESS(ES)</b> NASA Langley Research Center Hampton, VA 23665-5225		<b>8. PERFORMING ORGANIZATION REPORT NUMBER</b>	
<b>9. SPONSORING / MONITORING AGENCY NAME(S) AND ADDRESS(ES)</b> National Aeronautics and Space Administration Washington, DC 20546		<b>10. SPONSORING / MONITORING AGENCY REPORT NUMBER</b>  NASA TM-107620	
<b>11. SUPPLEMENTARY NOTES</b> Piascik: NASA Langley Research Center, Hampton, VA 23665-5225; Gangloff: University of Virginia, Materials Science and Engineering Department, Charlottesville, VA 22903			
<b>12a. DISTRIBUTION / AVAILABILITY STATEMENT</b>  Unclassified - Unlimited  Subject Category - 39		<b>12b. DISTRIBUTION CODE</b>	
<b>13. ABSTRACT (Maximum 200 words)</b> Based on a fractographic analysis of fatigue crack propagation (FCP) in Al-Li-Cu alloy 2090 stressed in a variety of inert and embrittling environments, microscopic crack paths are identified and correlated with intrinsic $da/dN-\Delta K$ kinetics. FCP rates in 2090 are accelerated by hydrogen producing environments (pure water vapor, moist air and aqueous NaCl), as defined in Part I. For these cases, subgrain boundary fatigue cracking (SGC) dominates for $\Delta K$ values where the crack tip process zone, a significant fraction of the cyclic plastic zone, is sufficiently large to envelop 5 $\mu m$ subgrains in the unrecrystallized microstructure. SGC may be due to strong hydrogen trapping at $T_1$ precipitates concentrated at sub-boundaries. At low $\Delta K$ , the plastic zone diameter is smaller than the subgrain size and FCP progresses along {100} planes due to either local lattice decohesion or aluminum-lithium hydride cracking. For inert environments (vacuum, helium and oxygen), or at high $\Delta K$ where the hydrogen effect on $da/dN$ is small, FCP is along {111} slip planes; this mode does not transition with increasing $\Delta K$ and plastic zone size. The SGC and {100} crystallographic cracking modes, and the governing influence of the crack tip process zone volume ( $\Delta K$ ), support hydrogen embrittlement rather than a surface film rupture and anodic dissolution mechanism for environmental FCP. Multi-sloped log $da/dN$ -log $\Delta K$ behavior is produced by changes in process zone hydrogen-microstructure interactions, and not by purely micromechanical-microstructure interactions, in contradiction to microstructural distance-based fatigue models.			
<b>14. SUBJECT TERMS</b> Environmental fatigue; Corrosion fatigue; Aluminum-Lithium; Hydrogen embrittlement; Crack tip modeling			<b>15. NUMBER OF PAGES</b> 33
			<b>16. PRICE CODE</b> A03
<b>17. SECURITY CLASSIFICATION OF REPORT</b> Unclassified	<b>18. SECURITY CLASSIFICATION OF THIS PAGE</b> Unclassified	<b>19. SECURITY CLASSIFICATION OF ABSTRACT</b>	<b>20. LIMITATION OF ABSTRACT</b>

